Refractive index sensing utilizing parallel tapered nano-slotted photonic crystal nano-beam cavities

Jian Zhou,[1] Huiping Tian,[1,3,*] Daquan Yang,[1,2] Qi Liu,[1] Lijun Huang,[1] and Yuefeng Ji[1,4]

[1]*The State Key Laboratory of Information Photonics and Optical Communications, School of Information and Communication Engineering, Beijing University of Posts and Telecommunications, Beijing 100876, China*
[2]*School of Engineering and Applied Sciences, Harvard University, Cambridge, Massachusetts 02138, USA*
[3]*Beijing University of Posts and Telecommunications, P.O. Box 90, #10 Xitucheng Road, Haidian District, Beijing 100876, China*
[4]*e-mail: jyf@bupt.edu.cn*
**Corresponding author: hptian@bupt.edu.cn*

Received March 31, 2014; revised May 28, 2014; accepted June 5, 2014; posted June 6, 2014 (Doc. ID 209244); published July 3, 2014

We demonstrate refractive index sensing using parallel tapered nano-slotted photonic-crystal nano-beam cavities with three-dimensional (3D) finite-difference time-domain (3D-FDTD) simulation. The electric field of the cavity mode is strongly concentrated in the slot region leading to a large light–matter overlap, which is expected to add a significant contribution to sensitivity, and thus we present high refractive-index sensitivity of more than 600 nm/refractive index units. Additionally, the quality (Q)-factor in the proposed design is theoretically investigated, and through tapering the diameter of the pores outside the Bragg mirrors in nano-beam cavities and the width of the adjacent nano-slots, an optimal Q-factor of 11770 is obtained. A high figure of merit (FOM = 4637) of the designed model has been obtained. We anticipate that this geometry is potentially an ideal platform for refractive-index based bio-sensing.

OCIS codes: (130.3120) Integrated optics devices; (230.5750) Resonators; (230.5298) Photonic crystals; (280.4788) Optical sensing and sensors.
http://dx.doi.org/10.1364/JOSAB.31.001746

1. INTRODUCTION

Over course of recent years, the development of micro- and nano-scale optical technologies for bio-detection [1–4] has shown tremendous progress, with research activities mainly focused on developing highly sensitive detection schemes. The most exploited schemes are based on the principle of interferometry [5–7], optical cavities [8–16], and surface plasmon resonance [17,18]. Besides, photonic crystal (PhC) cavities having dimensions of the order of optical wavelengths that can confine light strongly are very important for a variety of scientific and engineering detection applications. All kinds of optical cavity sensors based on PhC slabs, PhC nano-lasers, one-dimensional (1D) PhC microfluidic, 1D nano-beam PhC cavities, and air-slot PhC nano-cavities have been demonstrated [19–28]. In these sensors the figure of merit (FOM) has been used to analyze sensor characteristics. To compare the performance of optical resonance based sensors, the FOM is defined as [29]

$$\mathrm{FOM} = S/\Delta\lambda, \tag{1}$$

where S is the sensitivity of the slope of the peak wavelength value with respect to the refractive index (RI), RIU indicates the refractive index unit, and $\Delta\lambda$ is the FWHM that represents the full-width at half-maximum of the resonance. We define the quality (Q)-factor as follows [30]:

$$Q = \lambda_0/\Delta\lambda. \tag{2}$$

λ_0 is resonant wavelength that represents the wavelength corresponding resonant frequency. Therefore, according to Eqs. (1) and (2), Eq. (1) can be modified to be

$$\mathrm{FOM} = S \cdot Q/\lambda_0; \tag{3}$$

however, the trade-off between S and Q limits the FOM. To achieve higher S, the field largely extends into the holes to increase the field overlap with the surrounding media. Nevertheless, in order to achieve higher Q, the optical mode should remain spatially localized in a small area. Here, the sensing performance of extensive optical structures is evaluated and compared in Table 1. As seen, the sensitivities of most PhC-based sensors are generally around 100–350 nm/RIU at around a 1550 nm wavelength [7,23,25–27]. Meanwhile it can be found that an "air-slot" PhC nano-cavity [28] has obtained an enhanced S (~500 nm/RIU) while Q maintains a high level (~10^4). S in a nano-slotted structure [31–33] shows a great improvement with respect to regular PhC design corresponding directly to the large overlap of the mode field with the analyte. It is worth noting that Allsop *et al.* [19] demonstrated S of 3365 nm/RIU in surface plasmon resonance structure and Wang *et al.* [33] demonstrated S of 900 nm/RIU in slot double-beam waveguides; however, Q-factors are limited to 1000 in [19] and 700 in [33].

In order to overcome above drawbacks and realize simultaneously high Q and S, PhC nano-beam cavities (PCNCs) [34–36] are currently the subject of intense research interest because they possess a suite of attractive characteristics: high

Table 1. Comparison of Sensitivity, *Q*-Factor and FOM for Different Optical Sensing Systems

Reference	Type of Sensing System	Target Substance	Sensitivity (nm/RIU)	*Q*-factor (at Telecom Range)	FOM
Allsop *et al.* [19]	SPR (grating coupled)	Water	~3365	~10^3	~2182
Sumetsky *et al.* [20]	Capillary ring resonator	Water	~800	~100	~52
Dai and He [21]	Mach–Zehnder interferometer	Water	~2000	~500	~645
Beheiry *et al.* [22]	PhC slab	Water	~644	~3000	~1253
Mileńko *et al.* [7]	PhC fiber	Water	~115	~10^3	~75
Kita *et al.* [23]	PhC nano-laser	Water	~350	~3000	~682
Nunes *et al.* [24]	1D PhC microfluidic	Water	~836	~200	~108
Yang *et al.* [25]	PhC array	Water	~161	~3000	~313
Quan *et al.* [26]	1D nano-beam	Water	~100	~10^4	~645
Gylfason *et al.* [27]	Slot-waveguide ring resonator	Water	~240	~500	~78
Jágerská *et al.* [28]	Air-slot PhC nano-cavity	Water	~510	~6000	~1985
Zhou *et al.*	PTNS-PCNC	Water	~606	~11770	~4637

optical *Q*-factor, wavelength-scale effective mode volume, low effective mass, and small physical footprint. Integrated within planer photonic waveguide circuitry, PCNCs provide an ideal architecture for sensing applications.

In this paper, first we optimize PCNCs for reducing the propagation loss based on spatially modulating the gratings (holes radius) near the defect [15,37]. Gaussian field distributions are well-known functions that greatly reduce the coupling to radiation modes [38]. We present a systematic design of high-Q tapered hole-radius resonators where six periods on each side of the defect are tapered. Second, to achieve higher interaction between the light and the nonlinear material, it is possible to use slotted waveguides [38]. In combination with PCNCs, the field enhancement in the slot, and thus the enhanced sensitivity to refractive index change, has been exploited to create high-performance refractive index sensors. Therefore, we propose the parallel tapered nano-slotted PhC nano-beam cavity (PTNS-PCNC). We demonstrated that a PTNS-PCNC sensor can simultaneously possess high S exceeding 606 nm/RIU (at 1541 nm) and Q exceeding 11770, resulting in *FOM* of ~4637.

2. DESIGN OF PCNC

The schematic of the PCNC is shown in Fig. 1. It consists of an array of air-holes in decreasing radii, etched into a ridge waveguide. The waveguide is formed in a 220 nm thick silicon core layer that provides adequate optical isolation of the waveguide core from the silicon substrate. In order to obtain the required high performance in this device, the reasonable choice of cavity length, nano-beam width, and the combination of periodic mirror and tapered region hole diameters is necessary. The hole-to-hole distances are constant (defined as periodicity $a = 360$ nm). The structure is symmetric with respect to the center of cavity in Fig. 1. In contrast to the majority of other cavity designs, current structure has additional cavity length inserted between the two periodic mirrors (w_c) that is the distance between the two central holes, which is different from that of the rest of the structure (a). This design minimizes the cavity loss, and the power guides along the PCNC are more concentrated in the cavity. We report the use of mirrors having $N_P = 2$ periodically spaced holes with diameters of 230 nm. Gradually tapered hole arrangements with different diameters are designed to produce a significantly enhanced Q-factor value through reductions in propagation losses and scattering that occur locally at transitions outside the cavity. Such tapered hole arrangements are made to reduce losses associated with abrupt changes in the modal distribution at the interfaces between the periodic mirror sections and the nano-beam waveguide. The tapered radius region outside the periodic mirror has hole radii from $r_{i\text{-start}} = 140$ nm, i.e., $r_i = r_1 - 11 \times i$ (i increases from 2 to 3), $r_i = r_3 - 22 \times i$ (i increases from 4 to $i_{\max}$).

The intrinsic properties of different regions of the PCNC structures are studied by band-structure analysis with MPB [39]. The holes in the cavity row are tapered accordingly to provide a reliable in-plane field confinement in the x direction. The holes surrounding the cavity are shifted to tune the optical field profile such that the vertical radiation scattering is minimized [40]. Figure 2(a) shows the band structure of the TE-like modes for the radius of six different holes in the PCNC structure. In order to minimize the scattering loss and realize high-Q design, each situation should satisfy the matching dielectric-mode band-edge frequencies of the holes. Intuition suggests that to limit out-of-plane scattering, the band-edge frequency and spatial field profile should closely match those of the hole of PCNC [15,16]. Figure 2(b) shows the mode-edge frequency versus the hole radius r_i. The apparent reduction in bandgap (i.e., the difference between the upper edge and

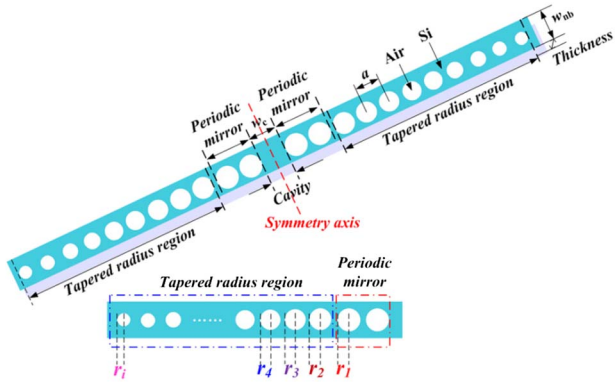

Fig. 1. Schematic of the proposed photonic crystal nano-beam cavity. The structure is symmetric with respect to its center (symmetry axis indicated by red dotted line). On both sides of the cavity, each mirror is composed of a periodic and tapered section. The periodic mirror is made of N_P holes ($N_P = 2$ in the figure). The taper is located on the periodic mirror side. a (~360 nm) is the center-to-center distance between the gratings (periodicity), w_c is the length of cavity. w_{nb} is the width of nano-beam. The thickness of nano-beam $T = 220$ nm. r_i are the radius of the gratings that are tapered from center to both ends.

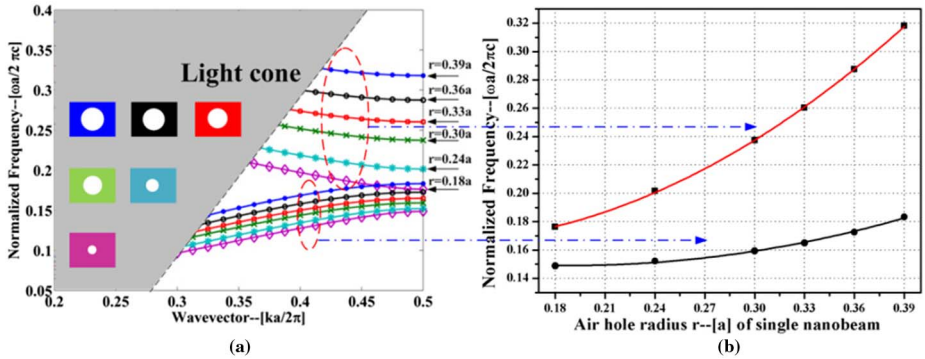

Fig. 2. (a) Band structures of the TE-like band for the nano-beam cavity with six different hole radii $r = 140$, 129, 118, 107, 85, and 63 nm, respectively. Unit cell geometries are shown in the inset. (b) Nano-beam bandadge frequency versus the nano-beam cavity hole radius r_i.

bottom edge for the certain hole radius) width with decreasing hole radius r_i is due to an effective decrease in the filling fraction or the ratio between air and dielectric regions in the unit cell. We also find that the edge of this guided band is pushed up as the hole radius increases and the almost zero overlap in frequency range [10] is important for suppressing the optical energy leakage via the PCNC. To further optimize the Q-factor, the modal distributions of the E_y component for different cavity lengths (w_c) and nano-beam widths (w_{nb}) are analyzed using 3D-FDTD simulation as shown in Fig. 3. It is clear that the electric field is concentrated in the center of the cavity when cavity length $w_c = 310$ nm and nano-beam width $w_{\mathrm{nb}} = 432$ nm so that it resembles a 1D cavity resonating along the center line as shown in Figs. 3(e) and 3(g). The E_y profile is given by the red solid line in Fig. 3(f), corresponding to 3(e).

From the band-structure design and the electric-field distribution analysis, we have created a localized cavity made by ensuring the in-plane modal confinement. In what follows we use the 3D-FDTD method to simulate the PCNCs and optimize their Q by increasing the number of unilateral air holes N. N is the total number of the periodic mirror (N_P) and tapered radius region (N_T). Figure 4 shows the simulation results for the resonant frequencies and Q-factors in terms of the number of unilateral air hole N. We have observed the desired results where the number of unilateral air holes increases, and the cavity resonance is pushed to higher frequencies because of the decrease in high-dielectric material in the PCNC structure. As seen in Fig. 4, the number of unilateral air holes $N = 7$

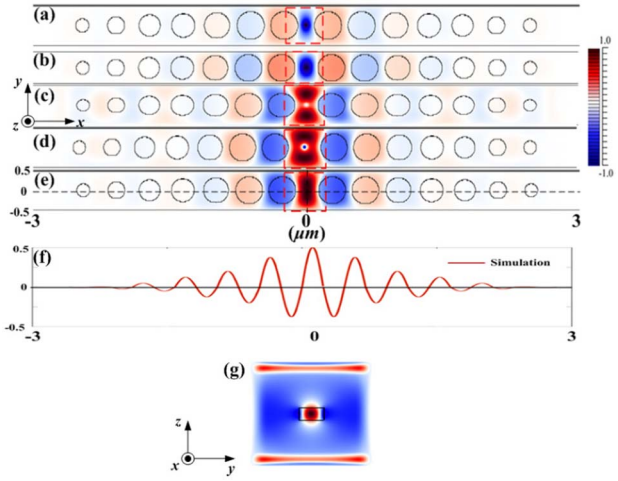

Fig. 3. E_y field distribution for the fundamental TE-like polarized light-wave in the x–y plane obtained from 3D-FDTD simulation with different cavity lengths (w_c) and nano-beam widths (w_{nb}). (a) $w_c = 274$ nm, $w_{\mathrm{nb}} = 432$ nm; (b) $w_c = 310$ nm, $w_{\mathrm{nb}} = 396$ nm; (c) $w_c = 310$ nm, $w_{\mathrm{nb}} = 468$ nm; (d) $w_c = 346$ nm, $w_{\mathrm{nb}} = 432$ nm; (e) $w_c = 310$ nm, $w_{\mathrm{nb}} = 432$ nm. (f) E_y field distribution along the dash line in (e), length unit, μm. (g) E_y field distribution for the fundamental TE-like polarized light-waves in the y–z plane corresponding to (e).

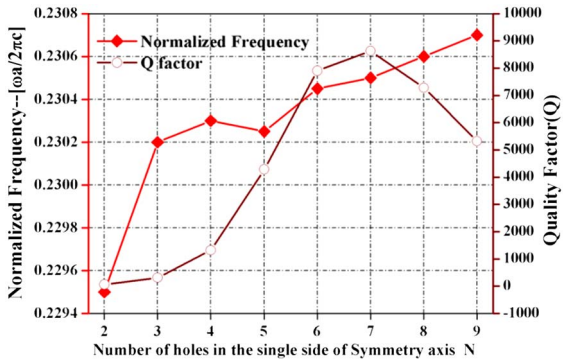

Fig. 4. 3D-FDTD calculations for the resonant frequencies and Q-factor as a function of the number of unilateral air holes N ($N = N_P + N_T$, $N_P = 2$, N_T is the number of tapered radius region).

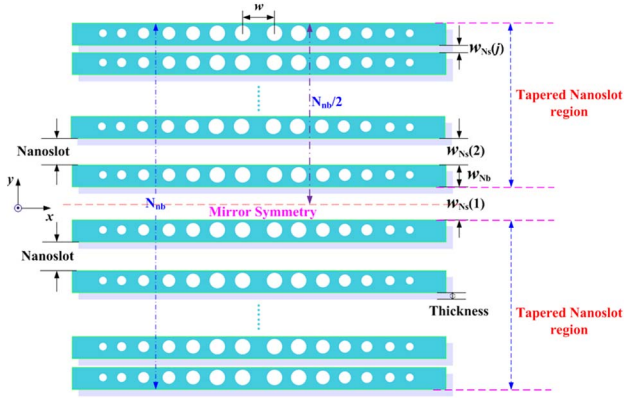

Fig. 5. Schematics of PTNS-PCNC that consists of multiple nano-beam with nano-slot separations. The structure is symmetric with respect to the center (mirror symmetry indicated by red dotted line). N_{nb} is the number of nano-beams, w is the center-to-center distance between the holes around the cavity. w_{nb} is the width of single beams. $w_{\mathrm{Ns}}(j)$ is the width of the nano-slot between adjacent beams.

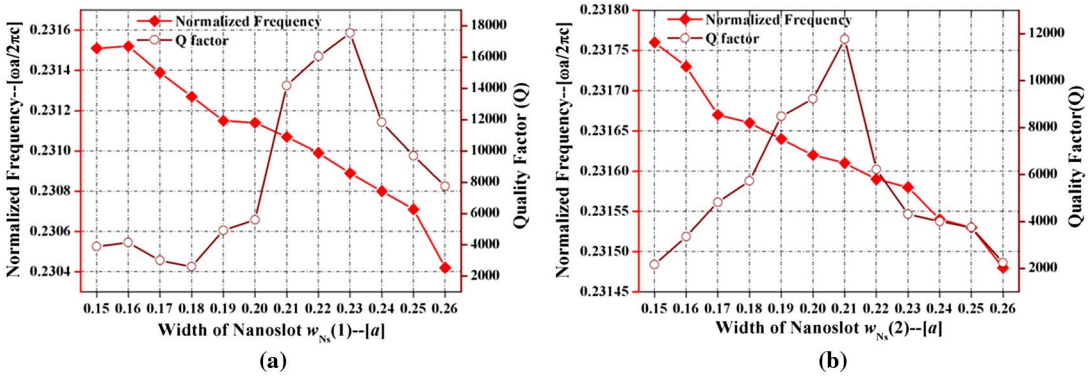

Fig. 6. Result of FDTD calculations displaying the cavity resonant frequencies and *quality* factors Q as a function of (a) the width of nano-slot w_{Ns} (1) when $N_{\mathrm{nb}} = 2$; (b) the width of nano-slot w_{Ns} (2) based on w_{Ns} (1) $= 0.23a$ when $N_{\mathrm{nb}} = 4$.

results in an optimal design at $(\omega = 0.23052(2\pi c/a))$ with a Q-factor of 8631. Based on the above design we set optimized parameters for the PCNC as follows: the length of cavity $w_c = 310$ nm, the width of nano-beam $w_{\mathrm{nb}} = 432$ nm, and the radius of the periodic mirror $r_1 = 140$ nm. The periodic tapered-radius region within the PCNC has radii (r_i, $i = 2$, 3, 4, 5, 6) of 129, 118, 107, 85, and 63 nm, respectively.

3. DESIGN AND OPTIMIZED SENSITIVITY OF PTNS-PCNC

The air-slot cavities have been investigated in [41,42]. Almeida *et al.* [41] proposed a new waveguide structure where two ridge waveguides are closely located with a nanometer size gap of low index so that the strong electric field is confined within the gap because of the large discontinuity of the field. Owing to the strong light–matter interaction, the slotted waveguide can be advantageously utilized in optical sensors. On the other hand, a slotted waveguide has been realized to control dispersion in PhCs, which also allows confining strong fields in the low-index gap [42]. Based on the above analysis, we propose a PTNS-PCNC as shown in Fig. 5, which consist of multiple parallel PCNCs with tapered nano-gap separations. $w_{\mathrm{Ns}}(j)$ (j increases from 1 to $j_{\max}$, $j_{\max} = N_{\mathrm{nb}}/2$, N_{nb} is the even integer) is the slot width of adjacent nano-beams. As the nano-slot width $w_{\mathrm{Ns}}(j)$ changes, the refractive index in the adjacent nano-beams changes. Thus, the resonant frequency of PTNS-PCNC will shift. As $w_{\mathrm{Ns}}(1)$ increases based on $N_{\mathrm{nb}} = 2$ from $0.15a$ to $0.26a$ with step size of $0.01a$, the calculated resonant frequencies and Q-factors as the function of the nano-slot width $w_{\mathrm{Ns}}(1)$ are shown in Fig. 6(a), obtained by using 3D-FDTD simulation. When the nano-slot width $w_{\mathrm{Ns}}(1)$ increases, the cavity resonance shifts toward lower frequencies. As seen in Fig. 6(a), the nano-slot width of $w_{\mathrm{Ns}}(1) = 0.23a = 83$ nm leads to an optimal design at $(\omega = 0.23091(2\pi c/a))$ with a Q-factor of 17546. Such high Q is most likely due to the fact that two nano-slot beams with a smaller elastic constant and a smaller mass apply less force to the anchor region and that the stress field is more localized with a reduced beam cross-sectional area [10]. These two factors lead to weaker residual loss (and thus higher Q). Next, we change the nano-slot width $w_{\mathrm{Ns}}(2)$, while fixing the nano-slot width at the optimum $w_{\mathrm{Ns}}(1) = 83$ nm based on $N_{\mathrm{nb}} = 4$. The resulting resonant frequencies and Q-factors calculated are shown in Fig. 6(b). As can be seen, the maximum Q-factor, as large as 11770 at $(\omega = 0.23061(2\pi c/a))$, is obtained for the nano-slot width $w_{\mathrm{Ns}}(2) = 0.21a = 76$ nm. In contrast to Fig. 6(a) we find that Q drops seriously for the increasing number of the nano-beams, there exist no confined mode. Thus we observe that the slot width between the adjacent nano-beams is linearly tapered from $w_{\mathrm{Ns}}(1) = 83$ nm, i.e., $w_{\mathrm{Ns}}(j) = w_{\mathrm{Ns}}(1) - 7 \times j$ (j increases from 1 to $j_{\max}$, $j_{\max} = N_{\mathrm{nb}}/2$). Beyond that we also investigate the dependence of Q on the slot thickness. As seen from Fig. 7, Q arrives at the climax when the slot thickness is 220 nm. When the slot thickness is lower than 100 nm, Q decreases because of the cut-off thickness of the fundamental TE mode. In addition, Q decreases when the slot thickness is larger than 300 nm. This is because the mode frequency becomes lower when the slot thickness increases and the lattice modulation of PTNS-PCNCs becomes gentle, which leads to reduced mode gap and thus results in weaken confinement and decreased the Q-factor [43].

In order to compare the sensitivity of the cavities at different resonances and Q-factors for different numbers of nano-beams, we define normalized sensitivity as $S_n = S/\lambda_0$. In the following discussion and simulation, the PTNS-PCNC surrounding media have indices that vary around the index of common liquid at telecom wavelength ($n_{\mathrm{liquid}} = 1.330$, $\lambda_0 = 1547$ nm). As shown in Fig. 8(a) we obtain normalized sensitivity (S_n) and Q-factor versus the number of nano-beams (N_{nb}). The sensitivity increases as N_{nb} increases and gradually saturates beyond $N_{\mathrm{nb}} = 6$. As N_{nb} increases, light is forced into the slot region as a result of the refractive index discontinuity [41]. When $N_{\mathrm{nb}} \geq 6$, most light has been strongly

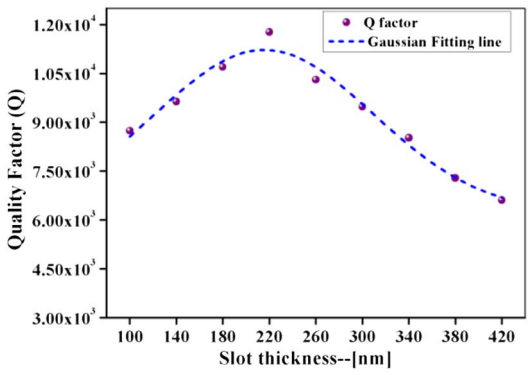

Fig. 7. FDTD simulation of Q factors in the PTNS-PCNCs as a function of the slot thickness.

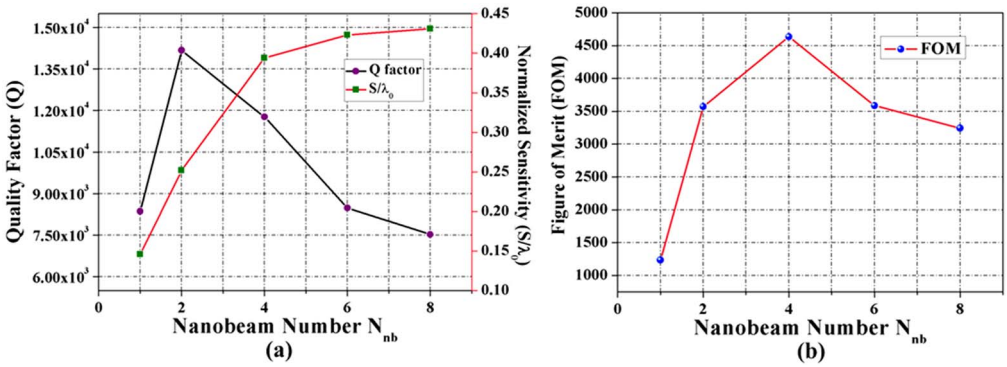

Fig. 8. (a) Normalized sensitivity (S/λ_0) and Q-factors as a function of the number of nano-beams (N_{nb}). (b) The FOM as a function of the number of nano-beams (N_{nb}).

squeezed in the slot region, and thus S approaches saturation. However, the Q-factor is degraded in the number of nano-beams ($N_{\mathrm{nb}} > 4$) due to the weak horizontal confinement. As a result of the trade-off between S_n and Q, the number of nano-beams $N_{\mathrm{nb}} = 4$ is selected to have $S_n \sim 0.394$ and $Q \sim 11770$ with the width of the nano-slots $w_{\mathrm{Ns}}(1) = 83$ nm, $w_{\mathrm{Ns}}(2) = 76$ nm. In Fig. 8(b), the FOM reaches climax when the number of nano-beams $N_{\mathrm{nb}} = 4$ and an optimized high FOM of 4637.4 has been obtained. As is expected from the slotted waveguide characteristics, it is clearly visible that most of the electric field profile (E_y) is confined within the slot of low-index material in the electric-field distribution along the y axis in Fig. 9. Eventually we also considered the effect of the fabrication roughness (e.g., hole radius offset) in our design. Our simulation was done assuming a random distribution of hole radii offset from −5 to 5, −10 to 10, −15 to 15, and −20 to 20 nm, respectively. As seen from Fig. 10, the Q-factor of 6×10^3–8×10^3 should be accepted when the fabrication perturbation is taken into consideration. In addition, the influence of the sensitivity has been calculated and the standard deviation is also evaluated approximately 12.3, that is, the obtained $S = 606.7 \pm 12.3$ nm/RIU.

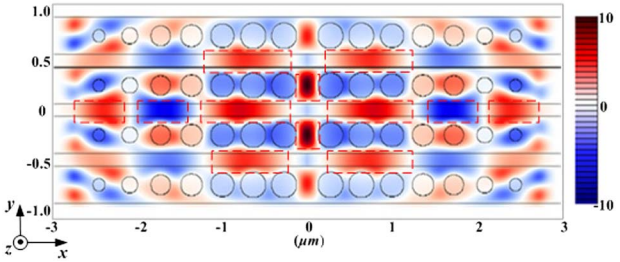

Fig. 9. 3D-FDTD simulation of the major field distribution profile (E_y) in the PTNS-PCNC. Here the number of Gaussian mirror segments $N = 14$, with an additional seven mirrors on both ends of tapering section. The calculation Q-factor is 11770 and the S factor is 606 nm/RIU. $a = 360$ nm, $w_{\mathrm{nb}} = 432$ nm, $w_c = 310$ nm, $T = 220$ nm, $w_{\mathrm{Ns}}(1) = 83$ nm, $w_{\mathrm{Ns}}(2) = 76$ nm. Unit of the x/y axis is μm.

4. SENSING CHARACTERISTIC OF PTNS-PCNCs

The above proposed PTNS-PCNC is one of the emerging configurations for refractive-index detection-based optical sensors due to unique properties simultaneously possessing high Q and high S. Alternatively, PTNS-PCNCs can also be coupled to on-chip optical network for high integration. In Fig. 11 we design a kind of coupler [44–46] that ridge the waveguide to introduce the light into the PTNS-PCNC structure as much as possible, with three ridge waveguides extruding to three nano-slots, respectively. Each beam of PTNS-PCNC "bites" with the ridge waveguide. Here, the width of the ridge waveguide w_{ridge} is 76, 83, and 76 nm, respectively. The thickness is kept at

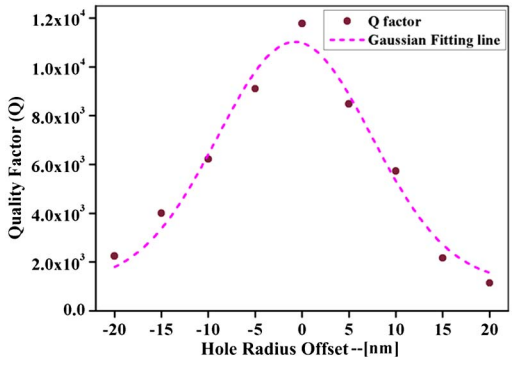

Fig. 10. FDTD simulation of Q-factors considering the effect of fabrication roughness. A random distribution of hole radius offset from −5 to 5, −10 to 10, −15 to 15, and −20 to 20 nm, respectively, are calculated. The cavity is immersed in an environment with a refractive index of 1.330.

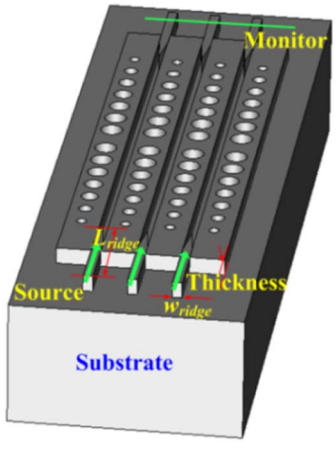

Fig. 11. Schematic diagram of the ridge waveguide used for the PTNS-PCNC sensor in/out coupling. The structure is symmetric with respect to the center.

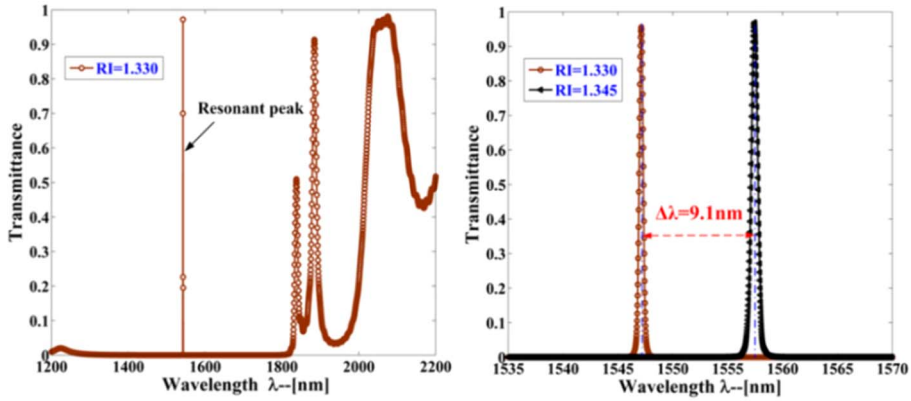

Fig. 12. (a) Transmission spectrum of PTNS-PCNC sensor from 3D-FDTD simulation. The simulation consists of three ridge waveguides extruding to three nano-slots, and the width of ridge waveguide w_{ridge} is 76, 83, and 76 nm, respectively. The thickness is kept at 220 nm. The length of ridge waveguide L_{ridge} is 1.5 μm. The background refractive index is set as RI = 1.330. A high Q of 11770 and near 100% transmission is obtained. (b) Shift of the resonant wavelength as the background index changes from RI = 1.330 to RI = 1.345.

220 nm. The length of ridge waveguide L_{ridge} is 1.5 μm. With 3D-FDTD simulation, we obtained the transmission spectrum of PTNS-PCNC, as light is launched from the ridge waveguide coupled into the PTNS-PCNC by the above-designed structure and finally collected from the output ridge waveguide. The total transmission spectrum is shown in Fig. 12(a). Since the mode shape of the nano-beam cavity is very similar to the waveguide mode, the coupling efficiency is relatively high enough to get a good transmission ratio while additional loss is not introduced by the existence of the ridge waveguides. A high Q around 11770 and near 100% transmission peak was observed. The modes at wavelengths lower 1360 nm and higher than 1650 nm are at the band edge modes. Figure 12(b) shows the shift of the fundamental TE-like mode when the refractive index changes from RI = 1.330 to RI = 1.345. The resonant wavelength shifted 9.1 nm. Thus, sensitivity $S = 606.7$ nm/RIU. In the case of the cost of reducing the on-resonance transmission, the current Q-factor should be further improved. However, the relatively high Q-factor and large S are expected while the transmission is kept the same.

5. CONCLUSION

In this paper we report on theoretical studies PTNS-PCNCs for high Q-factor and to measure high sensitivity (S) in the background material by 3D-FDTD simulation in the quadrabeam geometry. We fine-tuned the diameter of the circular gratings outside the Bragg mirrors in the single nano-beam cavity and widths of the adjacent nano-slots. The theoretically calculated Q-factors can be increased significantly, thus realizing a high Q of 11770. Because of a strong overlap of the cavity mode with the surrounding medium, such architecture can achieve a high sensitivity of 606.7 nm/RIU. It makes sense that we demonstrate a high FOM of 4637. In addition, we also investigated PTNS-PCNCs and found that it could be strongly coupled to the feeding waveguide with high efficiency with ridge-waveguide-to-PTNS-PCNCs couplers. Therefore, the proposed PTNS-PCNCs proved to very suitable for sensing biomolecules and could be also applied for medical or biological label-free sensing applications via proper functionalization. Simultaneously, it also would be a potential platform for making the sensor appropriately used for high-density integrated on-chip optical circuits. Furthermore, the obtained theoretical results are very promising for future experiments. We also anticipate that future experimental measurement will be better able to verify the calculated results.

ACKNOWLEDGMENTS

This research was supported by NSFC (No. 61372038), National 973 Program (No. 2012CB315705), National 863 Program (No. 2011AA010306), Postgraduate Innovation Fund of SICE, BUPT, 2013 and Fund of State Key Laboratory of Information Photonics and Optical Communications (Beijing University of Posts and Telecommunications) China.

REFERENCES

1. X. Fan, I. M. White, S. I. Shopova, H. Zhu, J. D. Suter, and Y. Sun, "Sensitive optical biosensors for unlabeled targets: a review," Anal. Chim. Acta **620**, 8–26 (2008).
2. W. C. Lai, S. Chakravarty, Y. Zou, and R. T. Chen, "Silicon nano-membrane based photonic crystal microcavities for high sensitivity bio-sensing," Opt. Lett. **37**, 1208–1210 (2012).
3. C. A. Barrios, M. Bauls, V. G. Pedro, K. B. Gylfason, B. Snchez, A. Griol, A. Maquieira, H. Sohlstrm, M. Holgado, and R. Casquel, "Label-free optical biosensing with slot-waveguides," Opt. Lett. **33**, 708–710 (2008).
4. H. K. Hunt and A. M. Armani, "Label-free biological and chemical sensors," Nanoscale **2**, 1544–1559 (2010).
5. J. Yang, L. Jiang, S. Wang, B. Li, M. Wang, H. Xiao, Y. Lu, and H. Tsai, "High sensitivity of taper-based Mach–Zehnder interferometer embedded in a thinned optical fiber for refractive index sensing," Appl. Opt. **50**, 5503–5507 (2011).
6. A. Ymeti, J. Greve, P. V. Lambeck, T. Wink, S. van Hovell, T. A. M. Beumer, R. R. Wijn, R. G. Heideman, V. Subramaniam, and J. S. Kanger, "Fast, ultrasensitive virus detection using a young interferometer sensor," Nano Lett. **7**, 394–397 (2007).
7. K. Mileńko, D. J. J. Hu, P. P. Shum, T. Zhang, J. L. Lim, Y. Wang, T. R. Woliński, H. Wei, and W. Tong, "Photonic crystal fiber tip interferometer for refractive index sensing," Opt. Lett. **37**, 1373–1375 (2012).
8. D. Yang, H. Tian, N. Wu, Y. Yang, and Y. Ji, "Nanoscale torsion-free photonic crystal pressure sensor with ultra-high sensitivity based on side-coupled piston-type microcavity," Sens. Actuators A **199**, 30–36 (2013).
9. J. O. Grepstad, P. Kaspar, O. Solgaard, I. R. Johansen, and A. S. Sudbø, "Photonic-crystal membranes for optical detection of single nano-particles, designed for biosensor application," Opt. Express **20**, 7954–7965 (2012).
10. X. Sun, J. Zheng, M. Poot, C. W. Wong, and H. X. Tang, "Femtogram dispersion L3-nanobeam optomechanical cavities: design and experimental comparison," Opt. Express **12**, 26486–26498 (2012).

11. V. Trivino, N. Rossbach, G. Dharanipathy, U. Levrat, J. Castiglia, A. Carlin, J. F. Atlasov, K. A. Butte, R. Houdre, and R. Grandjean, "High quality factor two dimensional GaN photonic crystal cavity membranes grown on silicon substrate," Appl. Phys. Lett. **100**, 071103 (2012).
12. A. Faraon, C. Santori, Z. Huang, V. M. Acosta, and R. G. Beausoleil, "Coupling of nitrogen-vacancy centers to photonic crystal cavities in monocrystalline diamond," Phys. Rev. Lett. **109**, 3604–3609 (2012).
13. T. Sar, J. Hagemeier, W. Pfaff, E. Heeres, S. Thon, H. Kim, P. Petroff, O. Tjerk, D. Bouwmeester, and R. Hanson, "Effect of a nanoparticle on the optical properties of a photonic crystal cavity: theory and experiment," J. Opt. Soc. Am. B **29**, 698–703 (2012).
14. B. T. Tung, D. V. Dao, T. Ikeda, Y. Kanamori, K. Hane, and S. Sugiyama, "Investigation of strain sensing effect in modified single-defect photonic crystal nanocavity," Opt. Express **19**, 8821–8829 (2011).
15. Q. Quan, P. B. Deotare, and M. Loncar, "Photonic crystal nanobeam cavity strongly coupled to the feeding waveguide," Appl. Phys. Lett. **96**, 203102 (2010).
16. Q. Quan and M. Loncar, "Deterministic design of wavelength scale, ultra-high *Q* photonic crystal nanobeam cavities," Opt. Express **19**, 18529–18542 (2011).
17. J. N. Anker, W. P. Hall, O. Lyandres, N. C. Shah, J. Zhao, and R. P. Duyne, "Biosensing with plasmonic nanosensors," Nat. Mater. **7**, 442–453 (2008).
18. C. Caucheteur, Y. Shevchenko, L. Shao, M. Wuilpart, and J. Albert, "High resolution interrogation of tilted fiber grating SPR sensors from polarization properties measurement," Opt. Express **19**, 1656–1664 (2011).
19. T. Allsop, R. Neal, S. Rehman, D. J. Webb, D. Mapps, and I. Bennion, "Generation of infrared surface plasmon resonances with high refractive index sensitivity utilizing tilted fiber Bragg gratings," Appl. Opt. **46**, 5456–5460 (2007).
20. M. Sumetsky, R. S. Windeler, Y. Dulashko, and X. Fan, "Optical liquid ring resonator sensor," Opt. Express **15**, 14376–14381 (2007).
21. D. Dai and S. He, "Highly sensitive sensor based on an ultra-high-*Q* Mach–Zehnder interferometer-coupled microring," J. Opt. Soc. Am. B **26**, 511–516 (2009).
22. M. E. Beheiry, V. Liu, S. Fan, and O. Levi, "Sensitivity enhancement in photonic crystal slab biosensors," Opt. Express **18**, 22702–22714 (2010).
23. S. Kita, K. Nozaki, and T. Baba, "Refractive index sensing utilizing a cw photonic crystal nanolaser and its array configuration," Opt. Express **16**, 8174–8180 (2008).
24. P. S. Nunes, N. A. Mortensen, J. P. Kutter, and K. B. Mogensen, "Refractive index sensor based on a 1D photonic crystal in a microfluidic channel," Sensors **10**, 2348–2358 (2010).
25. D. Yang, H. Tian, and Y. Ji, "Nanoscale photonic crystal sensor arrays on monolithic substrates using side-coupled resonant cavity arrays," Opt. Express **19**, 20023–20034 (2011).
26. Q. Quan, F. Vollmer, I. B. Burgess, P. B. Deotare, I. W. Frank, T. Sindy, K. Y. Tang, R. Illic, and M. Loncar, "Ultrasensitive on-chip photonic crystal nanobeam sensor using optical bistability," in *Quantum Electronics and Laser Science Conference (QELS)*, (May, 2011).
27. K. B. Gylfason, C. F. Carlborg, A. K. Zmierczak, F. Dortu, H. Sohlstrom, L. Vivien, C. A. Barrios, W. Wijngaart, and G. Stemme, "On-chip temperature compensation in an integrated slot-waveguide ring resonator refractive index sensor array," Opt. Express **18**, 3226–3237 (2010).
28. J. Jágerská, H. Zhang, Z. Diao, N. L. Thomas, and R. Houdré, "Refractive index sensing with an air-slot photonic crystal nanocavity," Opt. Lett. **35**, 2523–2525 (2010).
29. K. H. Yoon and M. L. Shuler, "Design optimization of nanograting surface plasmon resonance sensors," Opt. Express **14**, 4842–4849 (2006).
30. S. H. Kwon, T. Sünner, M. Kamp, and A. Forchel, "Optimization of photonic crystal cavity for chemical sensing," Opt. Express **16**, 11709–11717 (2008).
31. M. G. Scullion, A. di Falco, and T. F. Krauss, "Slotted photonic crystal cavities with integrated microfluidics for biosensing applications," Biosens. Bioelectron. **27**, 101–105 (2011).
32. A. di Falco, L. O'Faolain, and T. F. Krauss, "Chemical sensing in slotted photonic crystal heterostructure cavities," Appl. Phys. Lett. **94**, 063503 (2009).
33. B. Wang, M. A. Dündar, R. Nötzel, F. Karouta, S. He, and R. W. van der Heijden, "Photonic crystal slot nanobeam slow light waveguides for refractive index sensing," Appl. Phys. Lett. **97**, 151105 (2010).
34. I. Mukherjee, G. Hajisalem, and R. Gordon, "One-step integration of metal nanoparticle in photonic crystal nanobeam cavity," Opt. Express **19**, 22462–22469 (2011).
35. Z. M. Meng, Y. H. Hu, C. Wang, X. L. Zhong, W. Ding, and Z. Y. Li, "Design of high-*Q* silicon-polymer hybrid photonic crystal nanobeam microcavities for low-power and ultrafast all-optical switching," Appl. Phys. Lett. **426**, 1–10 (2013).
36. M. Geh, R. Gibson, J. Hendrickson, A. Homyk, A. Säynätjoki, T. Alasaarela, and Y. H. Lee, "Effect of atomic layer deposition on the quality factor of silicon nanobeam cavities," J. Opt. Soc. Am. B **29**, 55–59 (2012).
37. E. Kuramochi, H. Taniyama, T. Tanabe, K. Kawasaki, Y. G. Roh, and M. Notomi, "Ultrahigh-*Q* one dimensional photonic crystal nanocavities with modulated mode-gap barriers on SiO_2 claddings and on air claddings," Opt. Express **18**, 15859–15869 (2010).
38. Q. Xu, V. R. Almeida, R. R. Panepucci, and M. Lipson, "Experimental demonstration of guiding and confining light in nanometer-size low-refractive-index material," Opt. Lett. **29**, 1626–1628 (2004).
39. S. G. Johnson and J. D. Joannopoulos, "Block-iterative frequency-domain methods for Maxwell's equations in a planewave basis," Opt. Express **8**, 173–190 (2001).
40. Y. Akahane, T. Asano, B. S. Song, and S. Noda, "Fine-tuned high-*Q* photonic-crystal nanocavity," Opt. Express **13**, 1202–1214 (2005).
41. V. R. Almeida, Q. Xu, C. A. Barrios, and M. Lipson, "Ultracompact guiding and confining light in void nanostructure," Opt. Lett. **29**, 1209–1211 (2004).
42. A. Di Falco, L. O'Faolain, and T. F. Krauss, "Dispersion control and slow light in slotted photonic crystal waveguides," Appl. Phys. Lett. **92**, 083501 (2008).
43. M. Notomi, E. Kuramochi, and H. Taniyama, "Ultrahigh-*Q* nanocavity with 1D photonic gap," Opt. Express **16**, 11095–11102 (2008).
44. W. C. Lai, S. Chakravarty, X. Wang, C. Lin, and R. T. Chen, "On-chip methane sensing by near-IR absorption signatures in a photonic crystal slot waveguide," Opt. Lett. **36**, 984–986 (2011).
45. W. C. Lai, S. Chakravarty, X. Wang, C. Lin, and R. T. Chen, "Photonic crystal slot waveguide absorption spectrometer for on-chip near-infrared spectroscopy of xylene in water,"Appl. Phys. Lett. **98**, 023304 (2011).
46. Z. Han, A. Y. Elezzabi, and V. Van, "Wideband Y-splitter and aperture-assisted coupler based on sub-diffraction confined plasmonic slot waveguides," Appl. Phys. Lett. **96**, 131106 (2010).